

## Research Paper

**Cite this article:** Coomar S, Mondal S, Sanyal R (2022). Compact, flexible and highly selective wideband complementary FSS with high angular stability. *International Journal of Microwave and Wireless Technologies* **14**, 1298–1314. <https://doi.org/10.1017/S1759078721001707>

Received: 31 May 2021

Revised: 29 November 2021

Accepted: 30 November 2021

First published online: 27 December 2021

### Keywords:


Angular stability; complementary convoluted square loop; conformal; roll-off criterion; selectivity

### Author for correspondence:

Srimita Coomar,

E-mail: [srimita99@gmail.com](mailto:srimita99@gmail.com)

# Compact, flexible and highly selective wideband complementary FSS with high angular stability

Srimita Coomar<sup>1</sup> , Santanu Mondal<sup>1</sup> and Rajarshi Sanyal<sup>2</sup>

<sup>1</sup>Institute of Radio Physics & Electronics, University of Calcutta, Kolkata, India and <sup>2</sup>ECE Department, MCKV Institute of Engineering, Howrah, India

## Abstract

This article presents a novel miniaturized ( $0.105\lambda_0 \times 0.105\lambda_0$ ) flexible complementary frequency selective surfaces (CFSS) structure with sharp band edge selectivity and very high angular stability. To explore two diverse applications as a passband and stopband filter, a novel complementary convoluted square loop (CCSL) type structure has been designed and investigated on ultrathin dielectric material of thickness  $0.0023\lambda_0$ . The second-order wide controllable passband with fractional bandwidth of 19.23% ( $-3$  dB) and remarkably wide stopband of 64.7% ( $-10$  dB) and 54.8% ( $-20$  dB) respectively have been achieved by using a cascaded resonating structure which is composed of asymmetrical meandered CCSL array, arranged on two ultrathin dielectric layers with air foam separation. This particular format would lead to sharp band edge selectivity with steep roll-off (72.43 dB/GHz) and an excellent passband selectivity factor (0.731). An equivalent lumped LC circuit in conjunction with the transmission line model has also been adopted to comprehend the physical mechanism of the proposed single layer and double layer structures. Further, better passband and stopband angular stability at an oblique incident angle of  $45^\circ$  and the bending characteristics have also been investigated thoroughly for the proposed flexible CFSS to check their employability in different conformal structures with WiMAX passband and WLAN stopband application.

## Introduction

The complementary frequency selective surfaces (CFSS) are created by a periodic array of slots etched on the metallic surface and acronym as CFSS. Other than design simplification, the complementary structure offers very high angular stability [1]. The ultrathin and conformal CFSS attract the attention of researchers due to its versatile applicability in industrial, aerospace, commercial and medical sectors. The main goal of this work is to design and carry out investigations on the bandwidth enhancement characteristics, roll-off and selectivity of a planar and conformal ultrathin single layer as well as conformal double-layer CFSS to access its feasibility in modern applications.

Different effective design approaches have been proposed in early works related to convoluted and meandered geometry. In this regard, the convoluted dipole technique has been introduced in [2] to realize a longer current path. Here the long and narrow meandered metallic path in closer separation contributes to the resonant behavior. The Higher degree of meandering always leads to the raised inductive and capacitive values which are ultimately responsible for lower resonance frequency that motivates the structural miniaturization of the unit cell. An interwoven convoluted dipole has been proposed in ref. [3] to obtain the unit cell miniaturization. Similar structural geometry has been designed in [4] where a tortuous shaped metallic grid frequency selective surfaces (FSS) structure has been proposed to achieve miniaturized unit cell configuration. Miniaturization has also been carried out by a symmetrical spiral pattern of metallic meandered line geometry in a single layer FSS [5]. One double metallic layer related to tortuous has also been discussed in [6] where triangular spiral metallic FSS were cascaded with gridded tortuous to achieve triple passband with closer pole and zero separation. In [7], a cross grid structure has been proposed and investigated which would exhibit excellent passband selectivity. The convolution of metallic meandered pattern in each quadrant of the unit cell of single-layered FSS has been introduced in ref. [8] to achieve the closer separation between two transmission zeros. Another structural convolution technique between a basic rectangular shaped resonator and a synthetic resonator were presented in [9]. The meandered slotted curve design that poses the unit cell miniaturization with very high selectivity.

Miniaturization with a wide stopband was possible with interlocked 2.5D FSS [10]. A wide passband with more degree of freedom has provided the excellence of multilayer 3D FSS [11] though the complicated structural arrangement and a quite large assembling problem have extremely restricted the utilization of 3D FSS [12–14].

Bandwidth enhancement is an important issue in FSS structures. In this regard cascaded patch with a slotted ground plane is very significant work in recently reported works [15, 16]. Double layer Jerusalem cross-type CFSS array along with similar size Jerusalem patch array on the opposite layer dielectric substrate are mainly introduced to enhance the stopband characteristics [17]. The wide bandwidth of second-order passband has been realized by cascading the multiple layers of metallic mesh and its complementary structure in [18]. On the other hand, a wide tunable stopband could be achieved in simplified FSS geometry as discussed in [19, 20]. In [19], the interconnected coupling mechanism has been established, wherein [20], a shorted square loop exhibits the wide stopband range. The wide stopband has been achieved in [21] with the help of dual-layer FSS where the strategic cascading arrangement of the top and the bottom layer was taken into consideration. A controllable passband has also been recorded in [22] as the dielectric thickness varies.

In a straightforward manner, the higher-order enhanced passband or stopband filtering response with higher selectivity can be obtained by cascading multiple first-order bandpass or bandstop filters with  $\lambda/4$  air gap spacing where  $\lambda$  is the free-space wavelength. The air gap plays a key role to control the bandwidth or the order of filter characteristics. In ref. [23], two passband poles and three stopband zeros were generated with the help of a double layer asymmetrical square loop FSS array. Two layers were kept separated by substrate spacer  $\lambda/4$  air gap matching transformer. However, from a practical point of view, the optimized thickness or gap separations are rarely been maintained as traditional quarter-wave matching gap as discussed in [24, 25]. Third-order bandpass FSS using four layers of cascaded fractal metallic structure in [26] also comprises an overall thickness quite higher than  $\lambda/4$ . In contrary to the earlier context, numerous articles have reported the reduction of the air gap as well as the overall thickness well below the conventional quarter-wave matching gap. In this regard, a wide third-order stopband has been achieved in [27] where the maintained air gap separation is only  $\lambda/10$ . Another discussion of [28] has revealed the passband enhancement with second-order characteristics in dual-layer FSS system where a free space gap of  $\lambda/5$  between cascaded periodic layers was introduced. A similar investigation of [29] also mentioned the air space gap equivalent to  $\lambda/9$  to obtain second-order passband. Three metallic FSS were presented in [30] where two passband poles and two passband zeros were obtained without their gap matching. Hence the effective thickness was reduced significantly to  $\lambda/24$ . In a similar manner, three layers of fractal and complementary fractal FSS were strategically cascaded to realize a wide passband with three transmission poles where the effective thickness was approximately equivalent to  $\lambda/6$  [31].

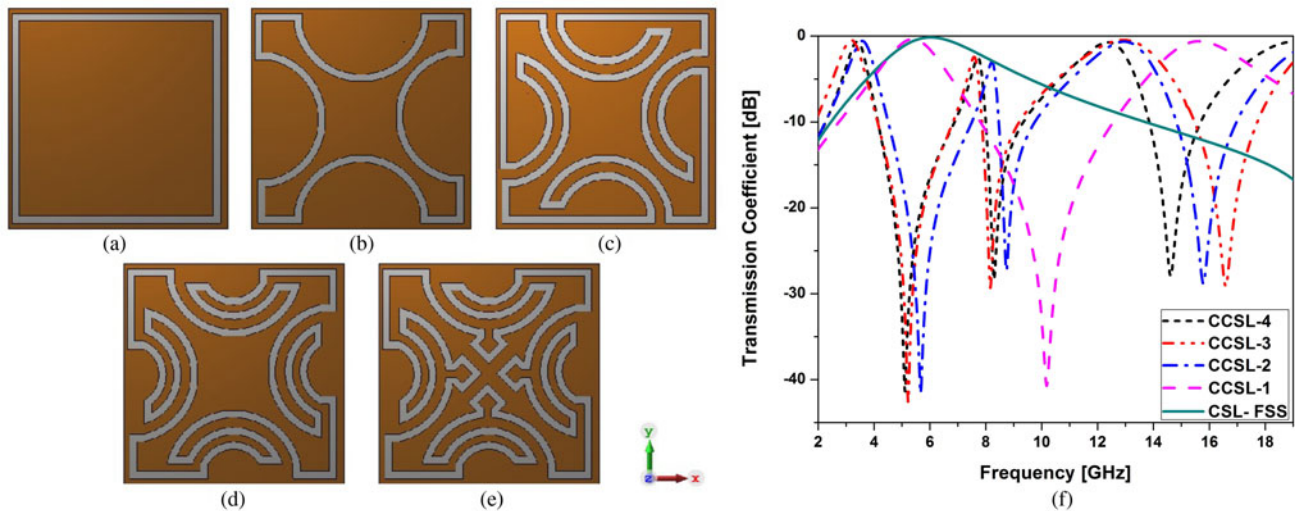
The transmission roll-off enhancement has also been discussed in [32] where the combination of a single square aperture structure and its complementary geometries has been considered in the proposed design. A novel approach of one-sided roll-off improvement was suggested in [33] using the interconnected array. However, the two-sided roll-off improvement is a crucial issue while passband selectivity is concerned. A high-selectivity FSS normally has a very narrow transition region between passband and stopband. Many techniques have been developed to design high-selectivity FSS, such as double-layer symmetrical element with the single substrate [34], multiple elements with the single substrate [35], multiple elements with multiple layers with air gap [7] or without air gap [36]. The selectivity improvement using 3D FSS configuration has also been proposed in some

previous works [14]. Although a large number of poles and zeros may be generated by 3D FSS, the design complication always creates a challenge in fabrication and in real-time applications. SIW may append the advantage of better selectivity as reported in ref. [37, 38]. Recently, flexible electronics are becoming a modern trend especially in the wireless communication industry and curved microwave devices are the prime requisition [39–41]. A very few research articles have proposed design approaches of conformal CFSS [17].

The study reported in this work presents the design and investigation of a miniaturized array element of ultrathin single layer CFSS structure with the planar and conformal characteristics. In order to emphasize the principle objective of a highly selective wide passband with two transmission poles and a sharp roll-off with second-order wide stopband, a double layer cascading of CFSS is suggested in the next phase of the proposed work. The novel and modified complementary convoluted square loop (CCSL) configuration is proposed to exploit the inherent unit cell miniaturization characteristics. An ultrathin dielectric material is incorporated to construct the single-layer CFSS. The fascinating feature of the modified CCSL design is its multiple meandered slotted path which not only leads to the cell miniaturization but also improves the roll-off. Increasing the number of meandered slot curves also improves the sharpness of the passband. Additionally, the inclusion of arrow-shaped slot in the design uniqueness shifts the passband transmission pole and the stopband transmission zero closer to each other which ultimately realizes the steep roll-off at the edge of the passband. The design synthesis based on the equivalent LC circuit model analysis of the proposed single CCSL structure has been derived from conventional filter theory. The filter parameters of lumped LC model are derived and determined from the simulated design specification of CST-MWS such as transmission poles and transmission zero of transmission coefficient and further validated by the ADS solver. Single-layer ultrathin dielectric is predicted as the cascaded lumped equivalent LC circuit comprises series inductance and shunt capacitance as derived from telegraph equation of electromagnetic wave [42]. The synthetic approach of the proposed double-layer cascaded configuration has been demonstrated by two similar lumped circuit models but different filter parameters of top and bottom CCSL structure. The dielectric layer and the air gap have been modeled with a short transmission line. The proposed single layer CCSL is configured as the top while the different geometry is considered for the bottom CCSL structure. Bottom CCSL has reduced the meandered slotted path without having the arrow-shaped slotted loop. This design optimization and air gap separation are unlike the traditional style of quarter wavelength matching. The top and bottom layers of the first order CCSL with ultrathin dielectric layers are kept separated by the approximation analytical technique at  $\lambda/8$  free space gap. The air gap spacing predominantly controls the coupling strength between two layers and hence is responsible for the fine-tuning of the bottom layer pole while the top layer pole remains constant and ultimately two successive poles in a close frequency separation introduce the flat and highly selective wide second-order passband response. Another exciting phenomenon is the adequate augmentation of the air gap to realize the prominent evolution of two stopband zeros of two different layers. The best compromise between the highly selective passband with 21% wide fractional bandwidth and the stopband occurs when the air gap separation is at  $0.098\lambda$ . The close proximity between the stopband nulls provides wide stopband rejection around 68% of the fractional

**Table 1.** Cell structure development vs parametric variation

Structures of development	Transmission poles ( $f_{p1}$ ) (GHz)	Transmission zeros ( $f_{z1}$ ) (GHz)	Frequency ratio ( $f_{z1}/f_{p1}$ )	Miniaturization characteristics (unit cell)	ROC (dB/GHz)
CSL-FSS	6.06	N/A	N/A	$0.18\lambda_0$	1.3
CCSL 1	5.4	10.14	1.88	$0.16\lambda_0$	4.73
CCSL 2	3.61	5.66	1.57	$0.107\lambda_0$	12.96
CCSL 3	3.21	5.23	1.63	$0.095\lambda_0$	12.28
CCSL 4	3.44	5.09	1.48	$0.101\lambda_0$	16.28

**Fig. 1.** Geometry of (a) CSL-FSS (b) CCSL-1 (c) CCSL-2 (d) CCSL-3 (e) proposed CCSL-4 (f) Transmission coefficient of Figs 1(a)–1(e).

bandwidth. This paper has been organized as follows: section “Design procedure of single layer CCSL-FSS” consists of single layer and double layer design principle, parametric investigation and synthesis including equivalent circuit model (ECM) for both the proposed structure. Section “Design and analysis of double-layered structure” describes the angular stability and bending characteristics of both structures. In the section “Angular stability of the proposed single and double-layered complementary FSS”<sup>4</sup>, the experimental verification for both the single and double layer structures are reported to validate the simulated results and finally, the overall conclusion is presented in section “Conformal behavior of Single and double layer complementary FSS”.

### Design procedure of single layer CCSL-FSS

This section comprises the design procedure of CCSL type FSS structure along with the parametric investigation and a lumped ECM in order to provide the physical interpretation of its performance as determined by the full-wave simulation results. Cell miniaturization and characteristics improvement is tabulated in Table 1.

### Unit cell geometry

A convoluted square loop slotted structure has been utilized to build this CFSS. The proposed geometry has been derived from

a complementary square loop (CSL). The next development regarding the improvement of electrical length has been accomplished by the sequential development of CCSL denoted as CCSL-1 to CCSL-4 as illustrated in Fig. 1. The geometrical configuration of the single-layered one side printed CCSL-4 design has been developed on ultrathin FR-4 substrate ( $\epsilon_r = 4.4$ ,  $h = 0.2$  mm &  $\tan\delta = 0.02$ ). The dimension of CCSL-4 unit cell configuration is  $0.105\lambda_0 \times 0.105\lambda_0 \times 0.0023\lambda_0$  ( $\lambda_0$  being the free space wavelength) which mainly contributes to achieving two narrow passbands separated by a wide stopband.

### Evolution of unit cell with design synthesis

In the design steps of the unit cell, initially, a narrow slotted square loop has been etched to the one-sided metallic surface which contributes to the hybrid  $L_2C_2$  resonator in parallel with the external wired grid and predicted as an inductor  $L$ . The transmission coefficient response of the CSL-FSS illustrates one transmission pole and one transmission zero as shown in Fig. 1(f). The impedance ( $Z$ ) of the above mentioned equivalent circuit of basic CSL-FSS can be expressed as

$$Z = \frac{j\omega L(1 - \omega^2 L_2 C_2)}{1 - \omega^2(L + L_2)C_2}$$

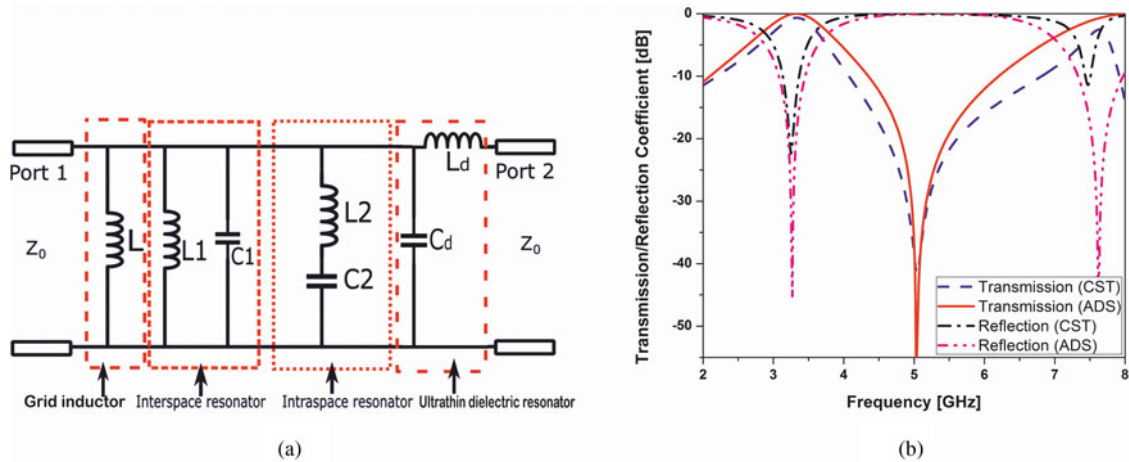


Fig. 2. (a) Equivalent circuit model of proposed single layer CFSS (CCSL-4) (b) Transmission and reflection coefficient of CST-MWS & ADS.

Hence the transmission pole ( $\omega_p$ ) and transmission zeros ( $\omega_z$ ) can be calculated as

$$\omega_p = \frac{1}{\sqrt{(L + L_2)C_2}} \tag{1}$$

and

$$\omega_z = \frac{1}{\sqrt{L_2C_2}} \tag{2}$$

Hence [2]

$$C_2 = \frac{1}{L_2\omega_z^2} \tag{3}$$

and

$$L = \frac{1}{C_2} \times \frac{\omega_z^2 - \omega_p^2}{\omega_z^2\omega_p^2} \tag{4}$$

The structural development of CCSL-1 provides the enhancement of the slotted length as shown in Fig. 1(b). The interspacing between the curved slots introduces an additional parallel resonating circuit  $L_1C_1$  while the intra spacing metallic part inside the four individual curved slots contributes largely to its capacitance of the series  $L_2C_2$  resonator. Hence the equivalent circuit of CCSL-1 can be empirical modeled as a parallel combination of  $L = 2.94$  nH,  $L_1 = 0.56$  nH,  $C_1 = 2.1$  pF are in parallel connection with series resonating circuit  $L_2 = 0.82$  nH,  $C_2 = 1.24$  pF as shown in Fig. 2(a). The fascinating feature of the transmission coefficient response of Fig. 1(f) shows that the modification of the CCSL structure development influences the shifting of the transmission zeros ( $\omega_z$ ) in the vicinity of the transmission pole ( $\omega_p$ ). Based on the ECM of Fig. 2(a), the transmission matrix of

CCSL geometry can be constructed as

$$\begin{bmatrix} A & B \\ C & D \end{bmatrix} = \begin{bmatrix} 1 & 0 \\ \frac{1}{j\omega L} & 1 \end{bmatrix} \begin{bmatrix} 1 & 0 \\ \frac{1}{j\omega L_1} & 1 \end{bmatrix} \begin{bmatrix} 1 & 0 \\ j\omega C_1 & 1 \end{bmatrix} \times \begin{bmatrix} 1 & 0 \\ \frac{1}{(j\omega L_2 + (1/(j\omega C_2)))} & 1 \end{bmatrix} \tag{5}$$

$$= \begin{bmatrix} 1 & 0 \\ \frac{1}{j\omega((L \times L_1)/(L + L_1))} & 1 \end{bmatrix} \begin{bmatrix} 1 & 0 \\ j\omega C_1 & 1 \end{bmatrix} \times \begin{bmatrix} 1 & 0 \\ \frac{1}{(j\omega L_2 + (1/(j\omega C_2)))} & 1 \end{bmatrix} \tag{6}$$

For simplification purpose, let  $L \times L_1/(L + L_1) = L_X$ ; hence the ABCD matrix can be written as

$$\begin{bmatrix} A & B \\ C & D \end{bmatrix} = \begin{bmatrix} 1 & 0 \\ \frac{(1 - \omega^2 L_X C_1)(1 - \omega^2 L_2 C_2) - \omega^2 L_X C_2}{j\omega L_X(1 - \omega^2 L_2 C_2)} & 1 \end{bmatrix} \tag{7}$$

Using the transformation between S parameters and ABCD parameters, the transmission coefficient ( $S_{21}$ ) between the two ports can be determined by using the reference [43]:

$$S_{21} = \frac{2Z_0}{AZ_0 + B + CZ_0^2 + DZ_0} \tag{8}$$

Where  $Z_0$  is the characteristics equation. In order to evaluate the passband pole  $|S_{21}| = 1$ , equation (8) can be rearranged as

$$\omega^4 L_X C_1 C_2 L_2 - \omega^2 (L_X C_1 + L_X C_2 + L_2 C_2) + 1 = 0. \tag{9}$$

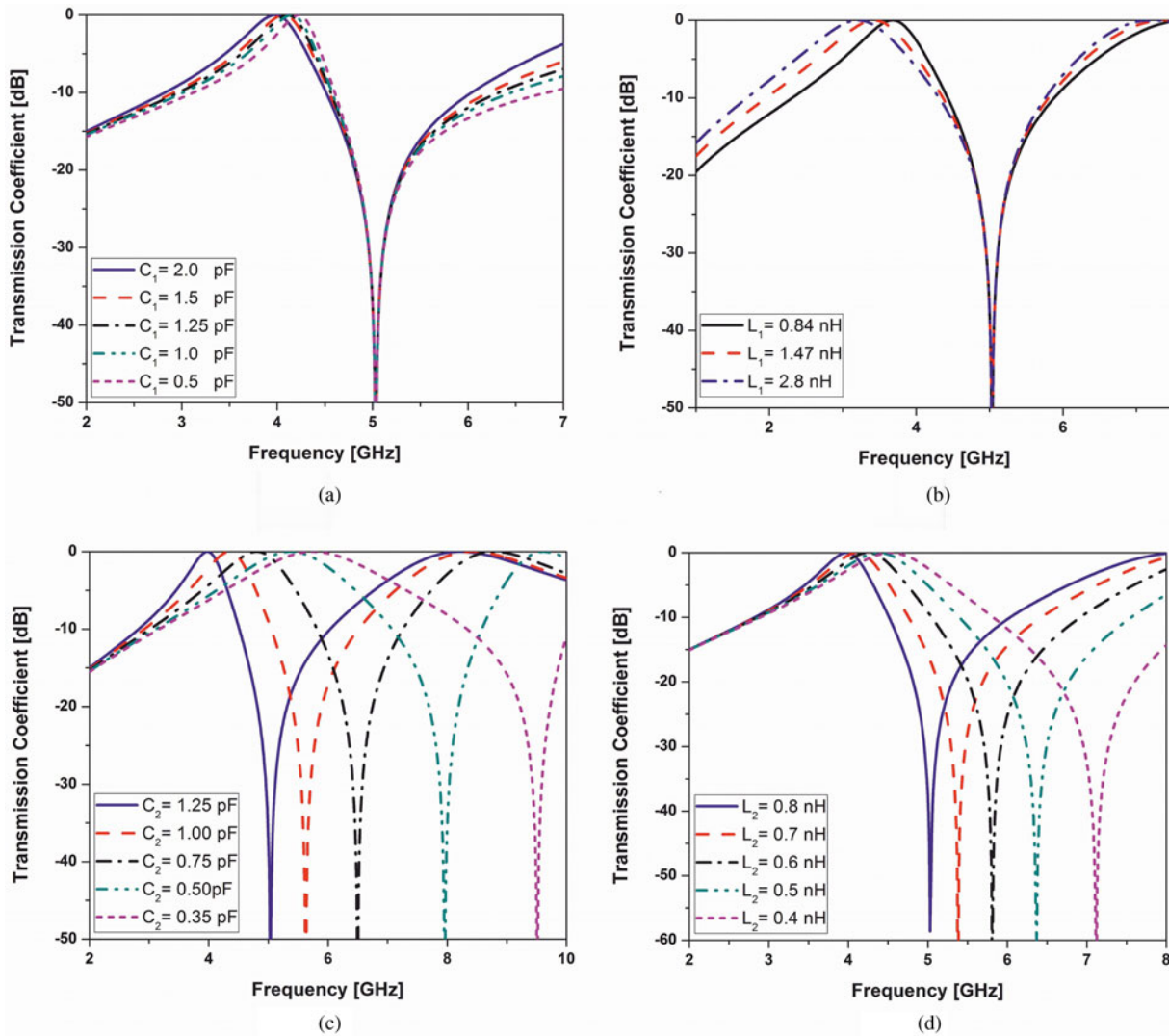


**Fig. 3.** Frequency response of Equivalent circuit with (a) varying  $C_1$  ( $L_1 = 0.56$  nH,  $L_2 = 0.82$  nH,  $C_2 = 1.24$  pF) (b) varying  $L_1$  ( $C_1 = 2.1$  pF,  $L_2 = 0.82$  nH,  $C_2 = 1.24$  pF) (c) varying  $C_2$  ( $L_1 = 0.56$  nH,  $C_1 = 2.1$  pF,  $L_2 = 0.82$  nH) (d) varying  $L_2$  ( $L_1 = 0.56$  nH,  $C_1 = 2.1$  pF,  $C_2 = 1.24$  pF).

Hence two poles  $\omega_{p1}$  and  $\omega_{p2}$  are

$$\omega_{p1} = \frac{\sqrt{(L_2 C_2 + L_X C_2 + L_X C_1) - \sqrt{(L_2 C_2 + L_X C_2 + L_X C_1)^2 - 4 L_X C_1 C_2 L_2}}}{2 L_X C_1 C_2 L_2} \tag{10}$$

$$\omega_{p2} = \frac{\sqrt{(L_2 C_2 + L_X C_2 + L_X C_1) + \sqrt{(L_2 C_2 + L_X C_2 + L_X C_1)^2 - 4 L_X C_1 C_2 L_2}}}{2 L_X C_1 C_2 L_2} \tag{11}$$

In order to determine stopband zero, the transmission coefficient  $|S_{21}| = 0$ . Hence the condition can be established as

$$j\omega L(1 - \omega^2 L_2 C_2) = 0 \text{ and } \omega_z = \frac{1}{\sqrt{L_2 C_2}} \tag{12}$$

The stopband zero completely depends on  $L_2$  and  $C_2$ . However, transmission poles are shifted with the varying  $L_1$ ,  $C_1$ ,  $L_2$  and  $C_2$  as illustrated in Fig. 3. According to the abovementioned expression of equations (8)–(11), the lumped equivalent circuit elements  $L_1$ ,  $C_1$ ,  $L_2$  and  $C_2$  can be expressed in terms of two poles and one zero as

$$L_2 = \frac{1}{\omega_z^2 C_2} \tag{13}$$

The design synthesis concerning poles is

$$(1 - \omega_p^2 L_X C_1) \times (1 - \omega_p^2 L_2 C_2) = \omega_p^2 L_X C_2 \tag{14}$$

Now, this equation can be modified as

$$(1 - \omega_p^2 L_X C_1) \times (\omega_z^2 - \omega_p^2) = \omega_p^2 \omega_z^2 L_X C_2 \tag{15}$$

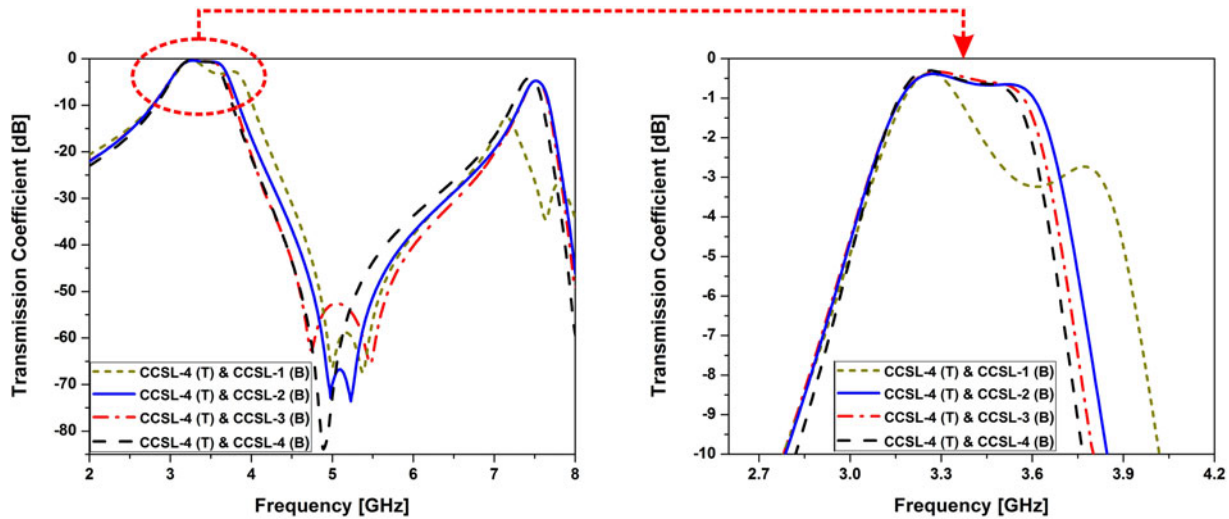


Fig. 4. Comparative transmission coefficient of different cascaded CCSL structure combinations.

Further rearranged expression is

$$\omega_p^4 L_X C_1 - \omega_p^4 (1 + \omega_z^2 L_X C_1 + \omega_z^2 L_X C_2) + \omega_z^2 = 0 \quad (16)$$

$$\omega_{p1}^2 = \frac{(1 + \omega_z^2 L_X C_1 + \omega_z^2 L_X C_2) + \sqrt{(1 + \omega_z^2 L_X C_1 + \omega_z^2 L_X C_2)^2 - 4 L_X C_1 \omega_z^2}}{2 L_X C_1}$$

$$\omega_{p2}^2 = \frac{(1 + \omega_z^2 L_X C_1 + \omega_z^2 L_X C_2) - \sqrt{(1 + \omega_z^2 L_X C_1 + \omega_z^2 L_X C_2)^2 - 4 L_X C_1 \omega_z^2}}{2 L_X C_1}$$

Replacing the value of  $L_X$ ,

$$C_1 = \frac{4 \omega_z^2}{((L \times L_1)/(L + L_1)) \left[ (\omega_{p1}^2 + \omega_{p2}^2) - (\omega_{p1}^2 - \omega_{p2}^2)^2 \right]}. \quad (17)$$

Here the optimum value of  $L$  can be determined from equation (4) of the CSL-FSS circuit model.  $L_1$  and  $C_1$  have been introduced due to the interspacing of slots. In order to synthesize both  $L_1$  and  $C_1$ , both the transmission pole and transmission zero are the key factors. However, the values of  $L_2$  and  $C_2$  of the lumped element model can be adjusted independently with  $\omega_z$ . In the further development of CCSL-2 and CCSL-3 geometry, the intra space meandered slot length increases in stepwise structural development and the narrow separation between the nearby meandered slots enhances the capacitive coupling effect which in turn enhances the value of  $C_2$ . On the other hand, the longer narrow metallic gap between etched curvatures is mainly responsible for large inductive cross-coupling. The enhanced inductive nature of the narrow metallic span maximizes  $L_2$ . Therefore, the shifting of poles and the zero toward the lower frequency can be observed in Fig. 1(f) and it can be validated by the ECM results as illustrated in Fig. 3 where the alteration of  $L_2$  and  $C_2$  sweep the position of zero though the poles position shifting is relatively lower. This variation illustrates a noticeable development of the frequency gap reduction between the primary transmission pole and transmission zero. This ultimately leads to the improvement of the roll-off criterion (ROC) of the right-handed slope of the passband. Since the magnitude of the transmission coefficient

(in dB) is varying with respect to the change of frequency (in GHz), therefore the ROC be defined as

$$ROC = \frac{\Delta_{dB}}{\Delta_{GHz}},$$

where,  $\Delta_{dB} = -3$  dB passband to  $-10$  dB stopband magnitude difference and  $\Delta_{GHz}$  is the difference between  $-3$  dB passband cut-off frequency to  $-10$  dB cut-off frequency in GHz.

In the proposed CCSL-4 structure, four arrow-shaped slotted extended loops are connected with each of four large slotted curvatures. These four symmetrical closer arrows shaped extended loop produce a very high capacitive coupling effect which results in the enhancement of  $C_1$ . As observed from Fig. 3 that the raised  $C_1$  value shifts transmission poles toward the lower frequency. However, the rate of shifting of the transmission pole is quite lower as compared to the variation of  $L_1$ . The inductive effect of the interspacing region deteriorates sharply which ultimately leads toward the sharp decrement of  $L_1$  and due to that a noticeable shifting of the primary pole of the transmission characteristics is observed. On the other hand, the frequency position of transmission zero is almost constant due to the negligible variation of  $L_2$ ,  $C_2$ , so that the gap between the primary pole and primary zero reduces significantly. In effect of that ROC of CCSL-4 becomes significantly high as compared to CCSL-3. The proposed CCSL-4 structure is mounted over an ultra-thin dielectric FR-4. The ultra-thin dielectric substrate of thickness  $h_1$  can be modeled in transmission line equivalent circuit as  $L_d C_d$  combination where,  $L_d = \mu_0 \mu_r h_1$ ,  $C_d = ((\epsilon_0 \epsilon_r h_1)/2)$  and " $\mu_0$ " is the free space permeability, " $\mu_r$ " is the relative permeability of the dielectric material, " $\epsilon_0$ " is the absolute permittivity and " $\epsilon_r$ " is the relative permittivity. To validate the abovementioned design, the synthesis procedure is carried on the calculated optimized parametric values of  $L = 2.94$  nH,  $L_1 = 0.56$  nH,  $C_1 = 2.1$  pF,  $L_2 = 0.82$  nH,  $C_2 = 1.24$  pF,  $L_d = 0.25$  nH and  $C_d = 0.15$  pF and the simulation is performed in ADS solver. The comparative transmission and reflection coefficient curves by CST electromagnetic solver and ADS simulation are illustrated in Fig. 2(b). It is observed that the curves agree with each other very well for  $\omega_{p1}$  and  $\omega_z$ . Although a little disagreement arises for  $\omega_{p2}$ , the discrepancy may be ignored.

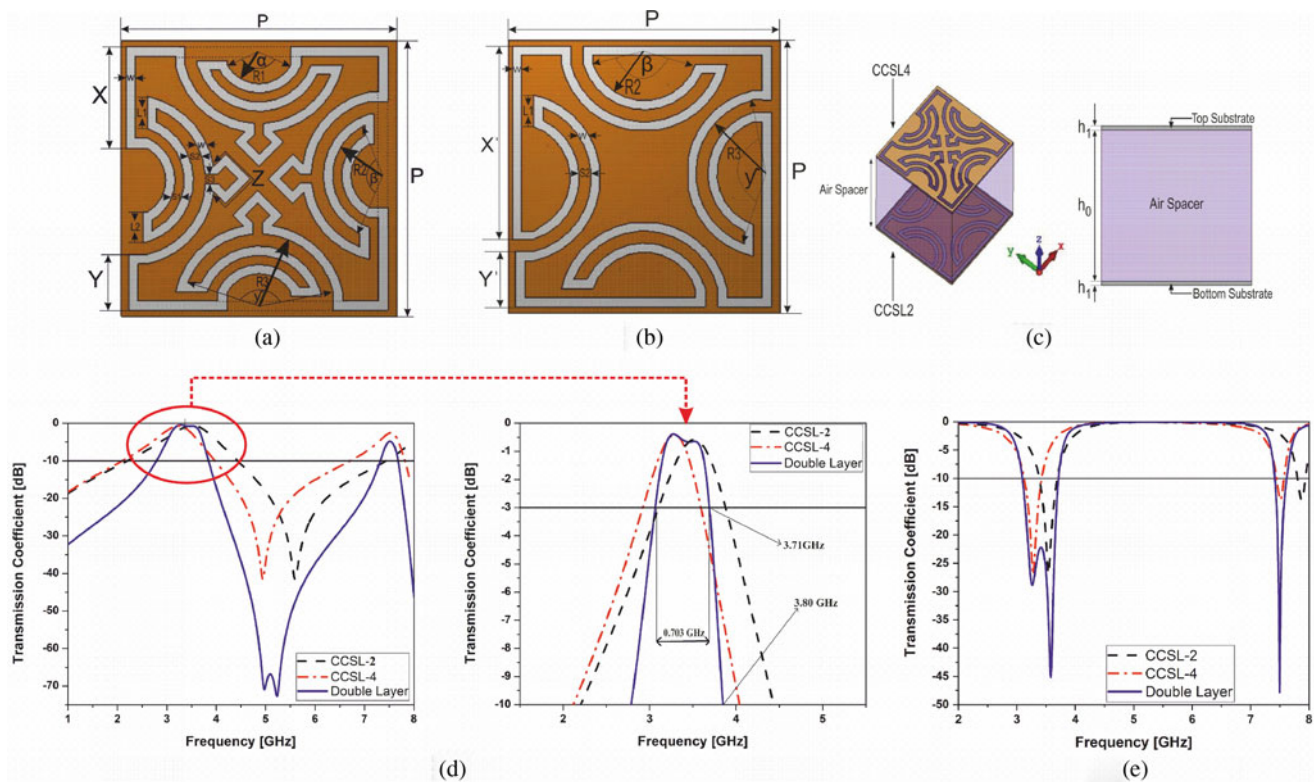


**Fig. 5.** Geometry of the proposed double layer (a) Top (b) Bottom (c) perspective & Side view and (d) Comparative Roll-off and Selectivity performance & (e) Reflection coefficient of individual CCSSL-4 (Top), CCSSL-2 (Bottom) and Proposed double layer.

### Design and analysis of the double-layered structure

Two single-layer CFSSs with free space separation can form a double-layer structure. In order to introduce the cascaded array of CCSSL structure on the top and the bottom of the double-layer CFSS with substrate spacer, a comparative transmission coefficient of different cascaded combinations has been illustrated in Fig. 4. This can be observed that the CCSSL-4 on both sides of the double layer has a flat passband response. A similar flat passband response can also be noticed for the combination of CCSSL4 and CCSSL-3 or CCSSL-4 and CCSSL-2. However, the fractional bandwidth of the passband for the CCSSL-4 and CCSSL-2 cascaded combination is approximately 20.35% which is comparatively better than the other two combinations. Apart from that, stopband for both-sided CCSSL-4 array has single transmission zero whereas two close transmission zeros of CCSSL-4 and CCSSL-2 combination introduces excellent second-order stopband characteristics. Moreover, the transmission coefficient of the CCSSL-4 and CCSSL-1 combination has also been demonstrated where passband response stability significantly deteriorates especially near the second transmission pole. Comparing the transmission coefficient response of the abovementioned CCSSL cascaded combination, the proposed double-layered structure with CCSSL-4 on the top layer and CCSSL-2 on the bottom layer along with a substrate spacer has been considered in the proposed double-layer CFSS as shown in Fig. 5.

### Topology and demonstration

High order mode coupling effects are ignored due to the simplification of the design synthesis. The main objective of this design

is to achieve a wide second-order passband response along with the wide second-order stopband response. The simulated transmission and reflection coefficient responses of Fig. 5(c) exhibit the two nearby transmission passband poles and also nearby stopband zeros. The air space ( $h_0$ ) between the ultrathin dielectrics is playing a key role where the increasing  $h_0$  certainly reduces the gap between two successive poles in order to maintain the flat and steep passband response with enhanced fractional bandwidth of 20.35%. Two successive passband poles are generated due to the top CCSSL-4 and bottom CCSSL-2. It can be noticed that the shifting of the second pole is completely controllable by varying the dielectric spacer length. Besides the magnitude of the second transmission pole improves significantly with the increasing air gap. The optimum air gap matching has been compromised to its maximum value of  $h_0 = 11$  mm which is equivalent to  $\lambda_0/8$  transmission line length where  $\lambda_0$  can be defined as the central passband frequency. At the optimized air gap separation, almost flat passband response has been realized with significantly sharp passband to stopband ROC as shown in Fig. 6. The peak magnitude of both the passband poles is above  $-1$  dB which illustrates the excellence of air gap coupling between top CCSSL-4 and bottom CCSSL-2 CFSS array. In addition to this, the steep passband could improve the passband Selectivity Factor (SF) which can be defined as

$$SF_{passband} = \frac{\text{Transmission Bandwidth}_{-3\text{dB}}}{\text{Transmission Bandwidth}_{-10\text{dB}}} \quad (18)$$

To improve passband SF, the proposed cascaded dual metallic layered CFSS structure helps in achieving wider bandwidth of the

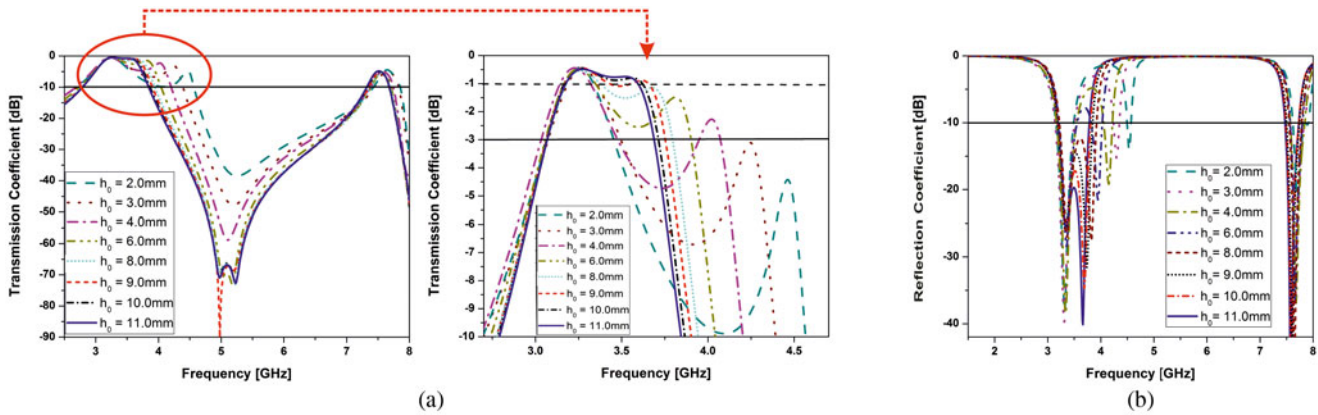


Fig. 6. Influence of air gap variation on frequency response on double-layer CFSS.

passband with higher-order response. Figures 5(d) and 5(e) illustrate the individual simulated transmission and reflection characteristics of the CCSL-2, CCSL-4 and the proposed dual-layer CFSS structure. The fascinating features of dual-layer structure as compared to independent ultrathin single-layer CCSL-2 or CCSL-4 are the enhanced passband (20.35%), enhanced stopband (63.5%), improved ROC (70 dB/GHz) and improved SF(0.692).

**Equivalent transmission line model of a double layer structure**

Figure 3 depicts a crucial feature of the increased  $C_2$  and  $L_2$  which is also responsible for the emergence of the sharp passband. This increasing sharpness lowers the passband SF. Dual-layer structure with free space may resolve this problem by generating the enhanced SF. The ultrathin dielectric substrate of thickness  $h_1$  on both sides of the air foam spacer sandwiched air space between the ultrathin dielectric can be modeled as a transmission line with characteristics impedance  $Z_0 = 377 \Omega$  with free space isolation gap  $h_0$ . The top complementary metallic structure is CCSL-4 and the bottom structure has been predicted as CCSL-2 has the impedance denoted as  $Z_T$  and  $Z_B$  respectively. CCSL-4 and CCSL-2 are mounted on ultrathin substrates of impedance

$$Z_d = \frac{Z_0}{\sqrt{\epsilon_r}}$$

where “ $\epsilon_r$ ” is the relative permittivity of the ultrathin substrate and  $Z_T$  can be expressed as

$$Z_T = \frac{j\omega L_X(1 - \omega^2 L_2 C_2)}{(1 - \omega^2 L_X C_1)(1 - \omega^2 L_2 C_2) - \omega^2 L_X C_2} \quad (19)$$

$$Z_B = \frac{j\omega L'_X(1 - \omega^2 L'_2 C'_2)}{(1 - \omega^2 L'_X C'_1)(1 - \omega^2 L'_2 C'_2) - \omega^2 L'_2 C'_2} \quad (20)$$

The single-layered ultrathin CFSS comprises CCSL-4 on the top of ultrathin dielectric material. The ABCD parameter of the subsection-1 of transmission line model shown

$$\begin{bmatrix} A_T & B_T \\ C_T & D_T \end{bmatrix} = \begin{bmatrix} 1 & 0 \\ \frac{1}{Z_T} & 1 \end{bmatrix} \begin{bmatrix} \cos \beta h_1 & jZ_d \sin \beta h_1 \\ \frac{j}{Z_d} \sin \beta h_1 & \cos \beta h_1 \end{bmatrix} \quad (21)$$

Since  $h_1$  is ultra-thin substrate thickness and hence it can be assumed that  $\sin \beta h_1 \approx 0$  and  $\cos \beta h_1 \approx 1$

$$\therefore \begin{bmatrix} A_T & B_T \\ C_T & D_T \end{bmatrix} = \begin{bmatrix} 1 & 0 \\ \frac{1}{Z_T} & 1 \end{bmatrix} \begin{bmatrix} 1 & 0 \\ 0 & 1 \end{bmatrix} = \begin{bmatrix} 1 & 0 \\ \frac{1}{Z_T} & 1 \end{bmatrix} \quad (22)$$

Similarly, the bottom CCSL-2 with the ultra-thin dielectric of subsection-2 can be simplified as

$$\begin{bmatrix} A_B & B_B \\ C_B & D_B \end{bmatrix} = \begin{bmatrix} 1 & 0 \\ \frac{1}{Z_B} & 1 \end{bmatrix} \quad (23)$$

Therefore ABCD of the transmission line model of dual-layer CFSS can be expressed as

$$\begin{bmatrix} A & B \\ C & D \end{bmatrix} = \begin{bmatrix} A_T & B_T \\ C_T & D_T \end{bmatrix} \begin{bmatrix} \cos \beta h_0 & jZ_0 \sin \beta h_0 \\ \frac{j}{Z_0} \sin \beta h_0 & \cos \beta h_0 \end{bmatrix} \times \begin{bmatrix} A_B & B_B \\ C_B & D_B \end{bmatrix} \quad (24)$$

Since in this work,  $h_0$  is approximated to  $\lambda/8$  on the stopband resonance in order to simplify, so that  $\beta h_0 = 2\pi h_0/\lambda = \pi/4$ , therefore rearranging equation (24), we have

$$\begin{bmatrix} A & B \\ C & D \end{bmatrix} = \begin{bmatrix} A_T & B_T \\ C_T & D_T \end{bmatrix} \begin{bmatrix} \frac{1}{\sqrt{2}} & \frac{jZ_0}{\sqrt{2}} \\ \frac{j}{\sqrt{2}Z_0} & \frac{1}{\sqrt{2}} \end{bmatrix} \begin{bmatrix} A_B & B_B \\ C_B & D_B \end{bmatrix} \quad (25)$$

Therefore equating the ABCD, we can solve the ultimate value of  $S_{21}$  from equation (4). In this regard, multiple simulations have been performed in ADS to extract the value of the parameters are  $L = 2.94 \text{ nH}$ ,  $L_1 = 0.56 \text{ nH}$ ,  $C_1 = 2.1 \text{ pF}$ ,  $L_2 = 0.82 \text{ nH}$ ,  $C_2 = 1.24 \text{ pF}$ ,  $L'_1 = 2.13 \text{ nH}$ ,  $C'_1 = 0.0187 \text{ pF}$ ,  $L'_2 = 0.7 \text{ nH}$ ,  $C'_2 = 1.12 \text{ pF}$ . It can be noted that  $C_1 > C'_1$  and  $L_1 < L'_1$  that indicates the noticeable reduction of metallic interspacing and intense capacitive coupling between four arrow-shaped slots. The comparative CST and ADS transmission coefficient depict the good agreement between those results with an excellent exhibition of two passband poles and two stopband zeros as depicted in Fig. 7(b).



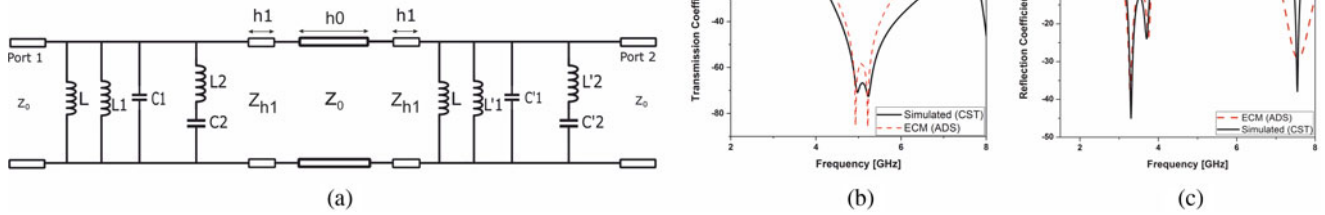


Fig. 7. (a) Equivalent circuit model of proposed double-layer CFSS (b) Transmission coefficient of CST-MWS & ADS (c) Reflection coefficient of CST-MWS & ADS.

**Angular stability of the proposed single and double-layered complementary FSS**

The simulated transmission coefficient of the proposed single-layered CCSL-4 structure and the proposed double-layered structure with different oblique incident angles for both TE and TM polarizations are illustrated in Figs 8 and 9 respectively. Excellent stability of passband and stopband response from 0°

to 60° can be observed for both the structures. A small deviation of primary zero 1.93% for 75° and 80° for a single layer can be seen. Otherwise, impressive frequency stability of CCSL-4 is due to the configurable symmetry of this miniaturized CCSL structure. However spurious resonance particularly for TM polarization arises especially for the transmission zero in higher incident angle is mainly due to the meandered loop design. The illustration

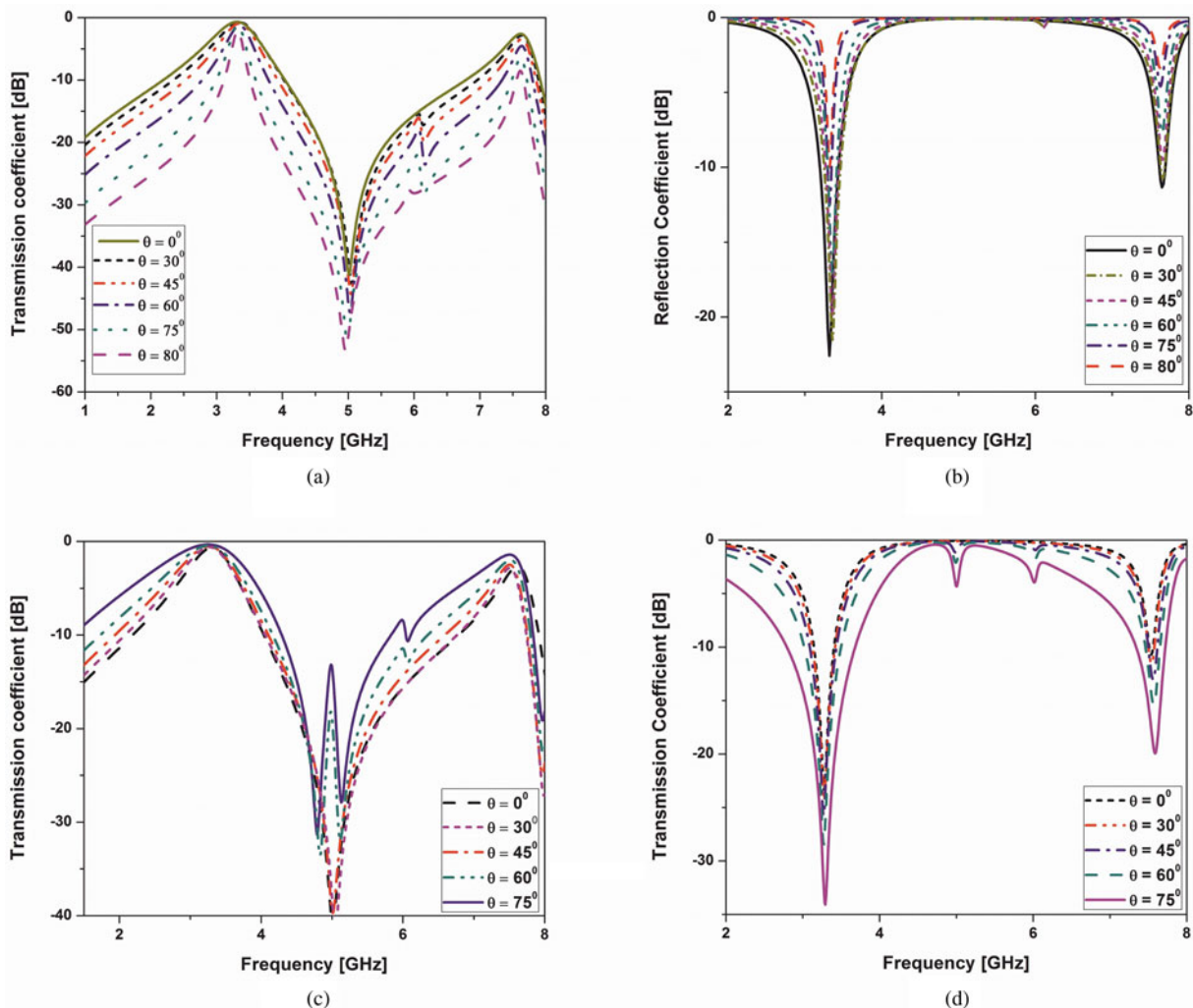
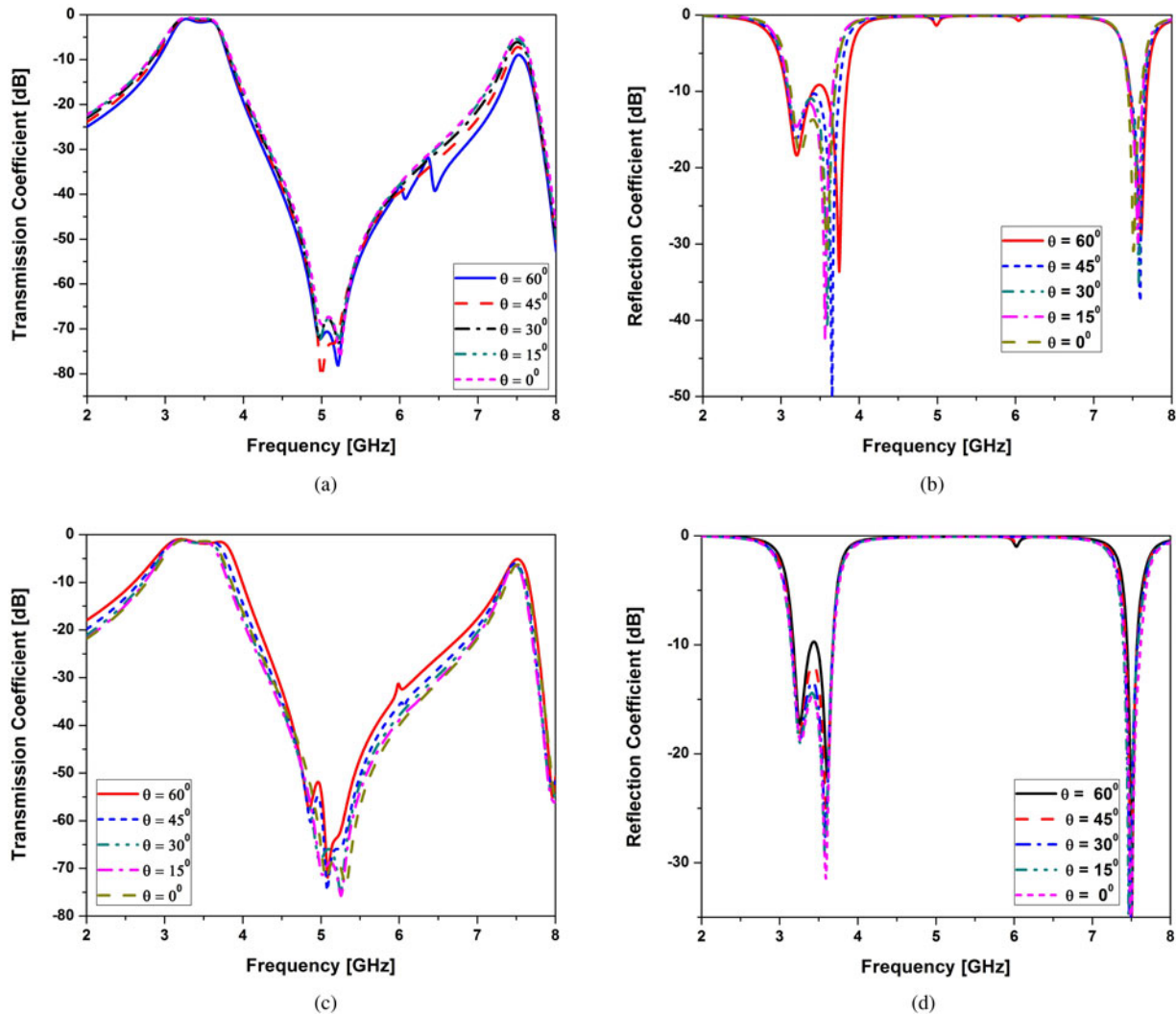


Fig. 8. Transmission and reflection coefficient of proposed single layer CFSS (CCSL-4) under different incident angle (a) Transmission (TE) (b) Reflection (TE) (c) Transmission (TM) (d) Reflection (TM).



**Fig. 9.** Transmission and reflection coefficient of proposed double layer CFSS under different incident angle (a) Transmission (TE) (b) Reflection (TE) (c) Transmission (TM) (d) Reflection (TM).

of the transmission coefficient of double-layered structure clearly indicates that the ripples near the two transmission zeros under a large oblique incident ( $\theta > 60^\circ$ ) especially for TM polarization are attributed to change of wave impedance. Similarly, it is observed that the flat top passband performance of TE polarization under different incident angles declines sharply for increasing incident angle ( $\theta > 45^\circ$ ). Besides, the bandwidth of the passband for TE polarization becomes sharper with the enlarging oblique incident angle. In the case of TM polarization on contrary, the bandwidth of passband increases with the increasing incident angle for both the single and dual-layer structure. This change is materialized due to the free space wave impedance.

In this context, it is worth investigating the sensitivity of its transmission coefficient response under different incident angles. The stability factor ( $F$ ) is the vital parameter to evaluate the pass-band sensitivity. In this regard, the stability factor ( $F$ ) can be investigated with respect to the normal and oblique incident as [1]

$$F = \sqrt{\frac{1}{N} \sum_{i=1}^N (T_{normal}(f_i) - T_{oblique}(f_i))^2} \quad (26)$$

where  $N$  is the total number of calculated frequency in the passband. The observation has been carried out for  $F$  with different incident angles for both the proposed single and dual-layered structures. It is worth mentioning that  $N=1$  has been opted for the CCSL-4 structure due to its single targeted primary pole resonance. Since the proposed dual-layer structure exhibits a wide flat passband response so that  $N=8$  has been predicted owing to the calculation accuracy purpose. After calculating it has been observed that  $F < 0.11$  for single layer and  $F < 0.18$  for dual layer at  $\theta_{max} = 60^\circ$  for TE polarization and significant stability can be observed for TM polarization where  $F < 0.016$  for both single and double layers at  $\theta_{max} = 60^\circ$ .

### Conformal behavior of single and double layer complementary FSS

For real-time applicability of the FSS, the curved form of the FSS becomes an essential part, particularly in Radom, aircraft or parabolic reflector. For such type of applicability, the bending effect investigation on FSS is a crucial issue. This article reveals the conformal feature of both the proposed single-layered CCSL-4 and the double-layered CFSS structure. The general perception always indicates that the performance characteristics of the planar and

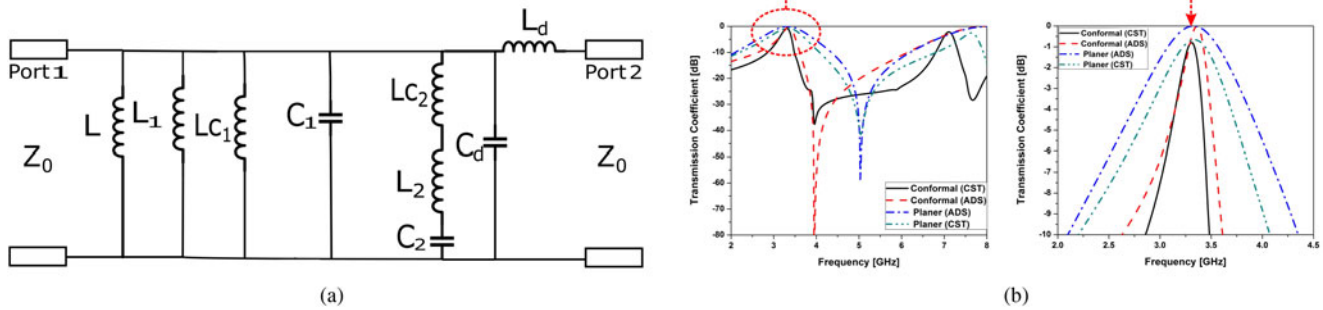


Fig. 10. (a) Modified ECM for conformal single-layer CFSS (b) Comparative transmission coefficient of CST-MWS & ADS for both planar and conformal FSS.

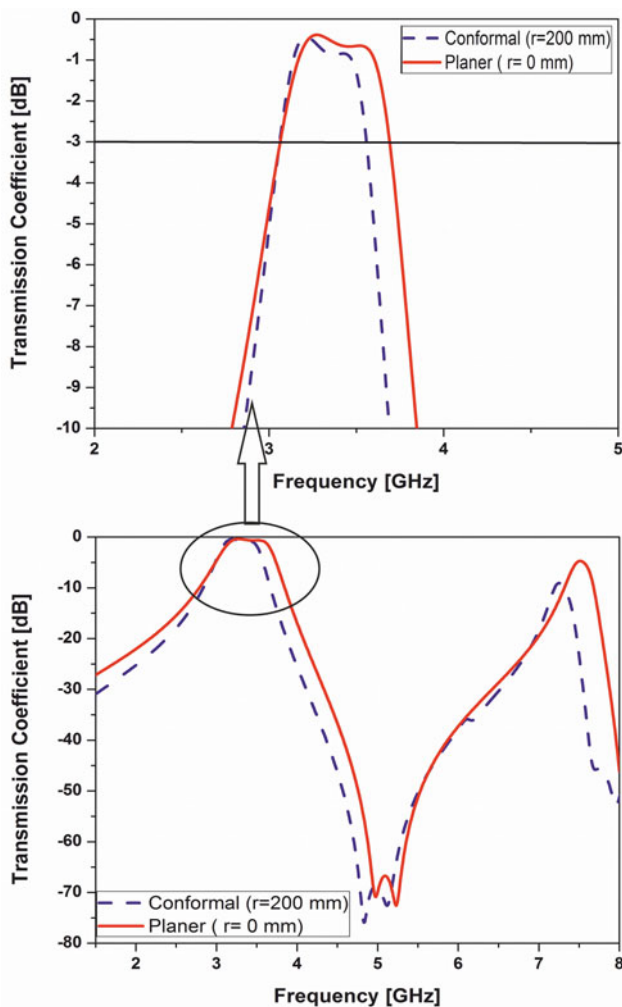


Fig. 11. Comparative transmission coefficient of the planar and conformal at normal incidence for double layer CFSS.

conformal should have similar performance characteristics. However, from a practical point of view, the justification of the conformal characteristics has two cornerstones: one is operating frequency and the other is the bandwidth [22]. The performance analysis by using CST-MWS electromagnetic solver set-up has been done by taking  $4 \times 4$  lattice of CCSL-4 unit cell. In this article, a slight bending degree has been considered with the larger vacuum cylindrical radius of  $r = 200$  mm. The cylindrical conformal structure is held perpendicular to the open boundaries along Z-axis on

Table 2. Optimized dimension of the parameters of proposed single and double layer CFSS

Parameters	Values
$P$ (mm)	9
$X$ (mm)	3.31
$Y$ (mm)	1.82
$X'$ (mm)	6.36
$Y'$ (mm)	1.82
$Z$ (mm)	3.26
$L_1$ (mm)	1.04
$L_2$ (mm)	0.97
$S_1$ (mm)	0.34
$S_2$ (mm)	0.46
$S_3$ (mm)	0.30
$W$ (mm)	0.30
$\alpha$ ( $^\circ$ )	133.07
$\beta$ ( $^\circ$ )	144.48
$\gamma$ ( $^\circ$ )	151.55
$R_1$ (mm)	1.05
$R_2$ (mm)	1.65
$R_3$ (mm)	2.34
$h_1$ (mm)	0.2
$h_0$ (mm)	11

the x-y plane to realize the structural symmetry. The added space is provided along the open boundary to suppress the higher-order modes. The specific circuit model analysis for the curved CFSS structure has been introduced to synthesize the lumped elements.

### Circuit model analysis of conformal single-layer complementary FSS

The comprehension of the bending mechanism can be assisted by the explanation and illustration of the modified ECM. The radius of curvature in the apex region of the convex curved surface is 200 mm has cell induced by the incident plane wave. The surface current distribution around the reduced circumference of the central element or apex region of the CCSL-4 array is highly influenced by the normalized plane wave on its slightly curved unit

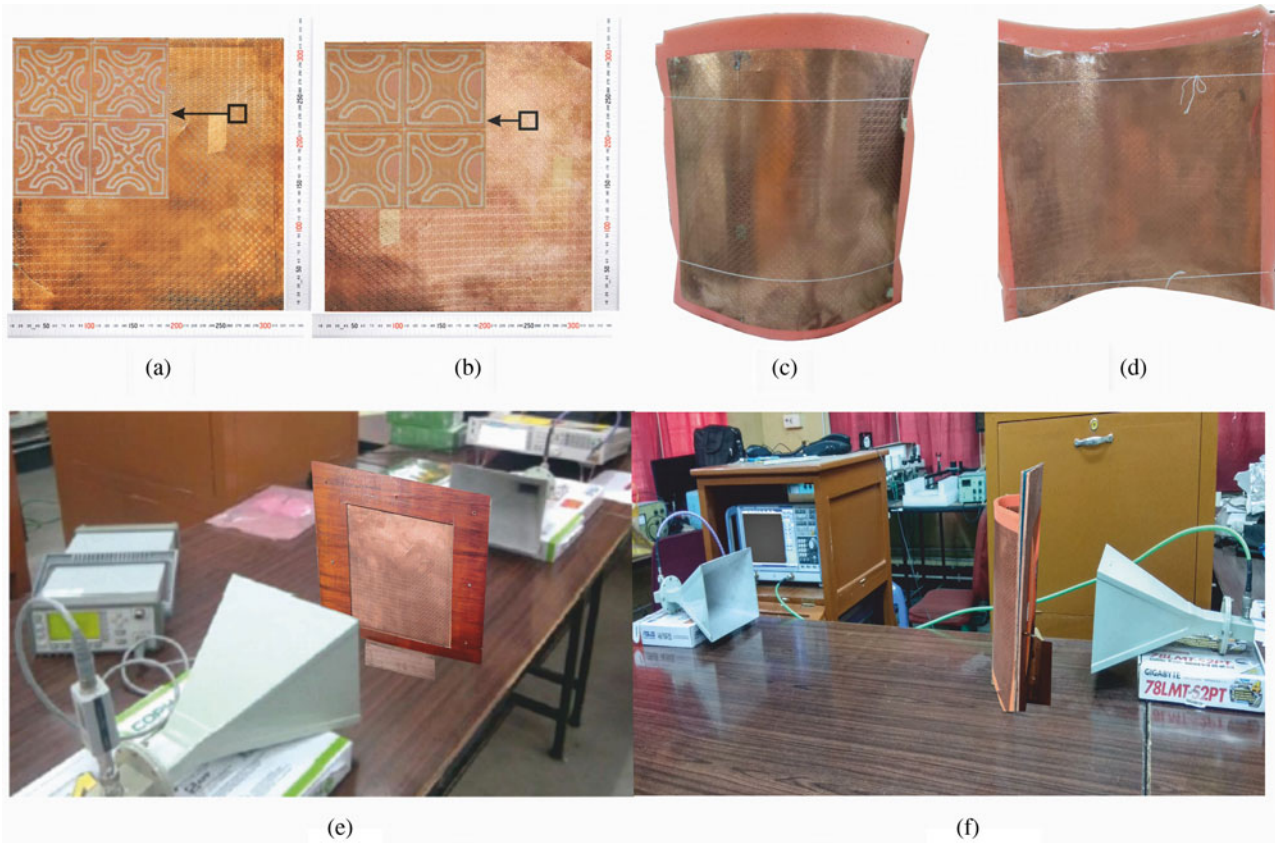


**Fig. 12.** Experimental verification of proposed CFSS (a) CCSL-4 prototype (Top) (b) CCSL-2 prototype (Bottom) (c) outward (d) inward curved double-layer structure (e) Free space measurement system for planar FSS (f) Free space measurement system for curved FSS.

cell area which has less circumference as compared to the planar one, which actually introduces the change of impedance due to the inclusion of the series inductive effect in the intra-spacing region. This series inductor ultimately shifted the transmission zero toward the lower frequency range. However, the angle of the incident to the nearby tilted cell array element on the curved CFSS is becoming large as compared to the planar CFSS, which creates an increasing phase difference in the magnetic field concerning the incident plane wave and therefore inter-element coupling among the unit cells are deteriorates noticeably. The weak coupling among the unit cell boundary contributes to the parallel inductive effect which is ultimately responsible for the sharpness of the passband [44, 45]. The shifting of transmission zero toward the pole ultimately enhances the ROC to 75.7 dB/GHz as compared to the planar structure with ROC 16.28 dB/GHz. However, the  $-3$  dB bandwidth of the passband of transmission coefficient is reduced significantly to 6.7% as compared to planar CCSL-4 of 23.75% as shown in Fig. 10(b). Figure 10 exhibits the modified equivalent circuit with additional lumped reactive components ( $L_{c1} = 0.55$  nH,  $L_{c2} = 0.5$  nH) and its corresponding transmission coefficient which clearly illustrates the better parity with the simulated result and validates the hypothesis regarding the conformal structure equivalent circuit.

#### Conformal structure of double-layered complementary FSS

The proposed double-layer conformal CFSS structure illustrates the little degraded fractional bandwidth of passband (16.51%) as compared to the planar structure passband (20.35%). On

contrary, conformal stopband (65.14%) is quite better as compared to stopband (63.5%). The passband to stopband one-sided ROC of the curved CFSS is 76.14 dB/GHz as compared to the planar double-layer structure (70 dB/GHz) as shown in Fig. 11. The SF of the double layer curved structure is 0.648 which is almost similar to the SF of planar (0.692). The study reveals that the passband and stopband responses of planar and conformal structures are almost in better agreement in spite of the little disagreement in ROC, passband and stopband regarding simulated transmission coefficient.

#### Experimental verification

The prototypes of CCSL-4 and the CCSL-2 have been fabricated in order to validate the simulated results of the proposed single and double layer CFSS structures as optimized parameters tabulated in Table 2. The proposed single layer CFSS structure is CCSL-4 with ultrathin FR-4 substrate and the proposed double-layer structure comprises of CCSL-4 and CCSL-2 complementary structures with two ultrathin substrates separated by air foam ( $\epsilon_r \approx 1$ ) as shown in Fig. 12.

#### Measurement setup

The measurement of the transmission coefficient of proposed single and dual-layer fabricated prototypes have been carried out by using two horn antenna setup pair are connected to a network analyzer (Rohde & Schwarz ZND20). Two types of horn antennas pair for different frequency ranges are utilized in the laboratory as

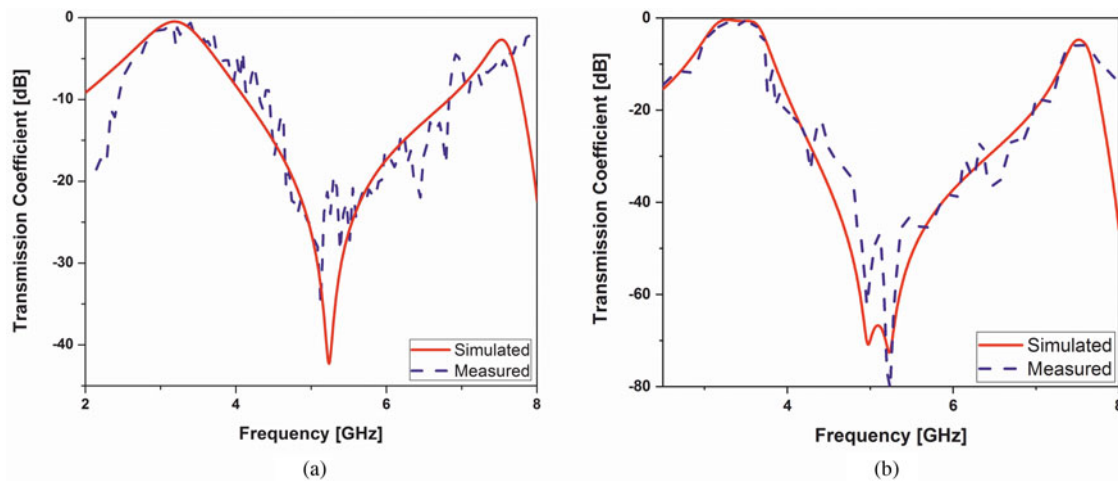


**Fig. 13.** Simulated vs Measured frequency response of planar (a) single layer (b) double layer CFSS array.

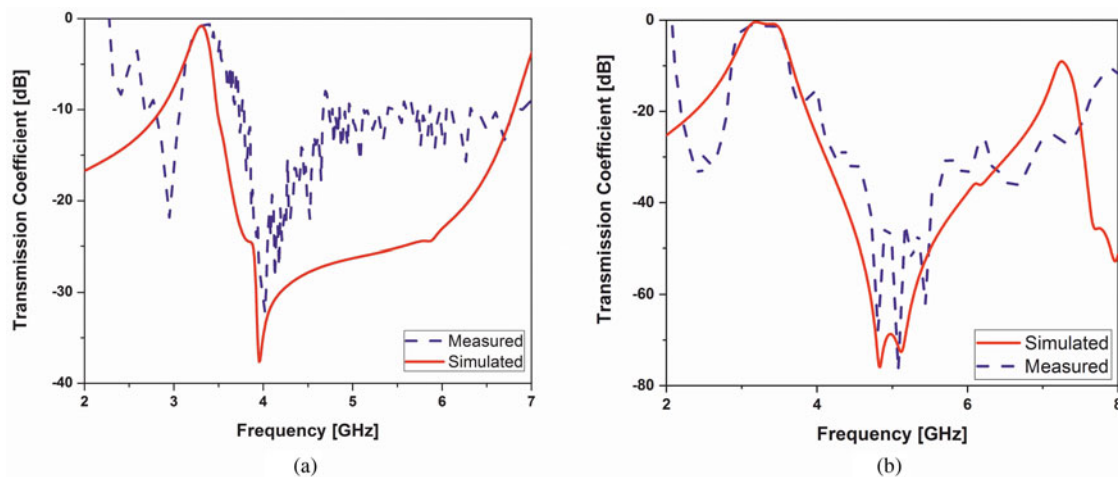


**Fig. 14.** Simulated vs Measured frequency response at normal incidence of conformal (a) single layer (b) double layer CFSS array.

transmitter and receiver measurement setup separately. The assigned frequency ranges of these antennas are 2–4 GHz and 4–8 GHz. Each antenna pair has a different flared cross-sectional area. Passband and stopband measurement for both the planar and conformal structure has been accomplished with the help of transmitter/receiver antenna setup with 2–4 GHz and 4–8 GHz correspondingly. Besides, the power sensor and power meter have also been incorporated along with the horn antenna to evaluate side lobe radiation. It has been observed that the abovementioned antenna setup uses with different specific frequency ranges made the side lobe radiation insignificant. Initially, calibration of setup has to be ensured with the transmission coefficient measurement without placing the CFSS array. The Horn antenna of the measurement setup is so arranged that it ensures the separation distance  $\geq 2D^2/\lambda$  where  $D$  is the maximum dimension of the antenna and  $\lambda$  denotes the operating wavelength [31].

Since the flexible nature of ultrathin single layer CCSL-4 generates misalignment for the normal incident, the air foam sheet along with wood frame fixture for measurement support is taken carefully to accomplish adequate measured results. The single-layer measurement has been carried out for a one-sided metallic CCSL-4 CFSS array. The single-sided conductor part of CCSL-4 is directed toward the transmission antenna. Due to the availability issue of an anechoic chamber, some new

mechanisms have been adopted to measure the transmission coefficient in free space. The FSS array has been placed in a wood frame where the rear part of the wooden fixture is completely embedded with an electromagnetic wave absorber material sheet in order to prevent the reflected ray effectively back to the antennas. The wide periphery of the wooden frame with wave absorbing sheet may also reduce the multipath effect. The planar FSS array has been placed approximately at the midpoint in between the transmission and receiving horn antenna gap in order to measure the transmission coefficient at the normal and oblique incident with  $\theta = 45^\circ$ . However, measurement regarding the conformal structure has been carried out in such a way that the position of the FSS array has been moved closer to the receiving horn antenna without any separation changes between the transmitting horn and receiving horn antenna. Therefore the flared cross-sectional aperture area can entirely cover the aperture area of curved FSS circumference thus collecting radio waves of the main lobe more efficiently and simultaneously avoiding the multipath effect.

### Measured results

The comparative simulated and measured transmission coefficient of single and double layer structures in both the planar

**Table 3.** Comparative simulated and measured values

Types	Planer single layer	Conformal single layer	Planer double layer	Conformal double layer
Simulated pass band (%)	23.75	6.7	20.35	16.51
Measured pass band (%)	23	9.2	19.23	15.14
Simulated -10 dB stop band (%)	68	64.91	63.5	65.14
Measured -10 dB stop band (%)	66.3	57.62	64.7	74.46
Simulated -20 dB stop band (%)	18.86	54.54	54.8	57.14
Measured -20 dB stop band (%)	19.22	4.89	53.2	59.4
Simulated ROC (dB/GHz)	16.28	75.7	70	76.14
Measured ROC (dB/GHz)	8.2	38.86	72.43	76.8
Simulated SF	0.33	0.346	0.692	0.648
Measured SF	0.41	0.492	0.731	0.79

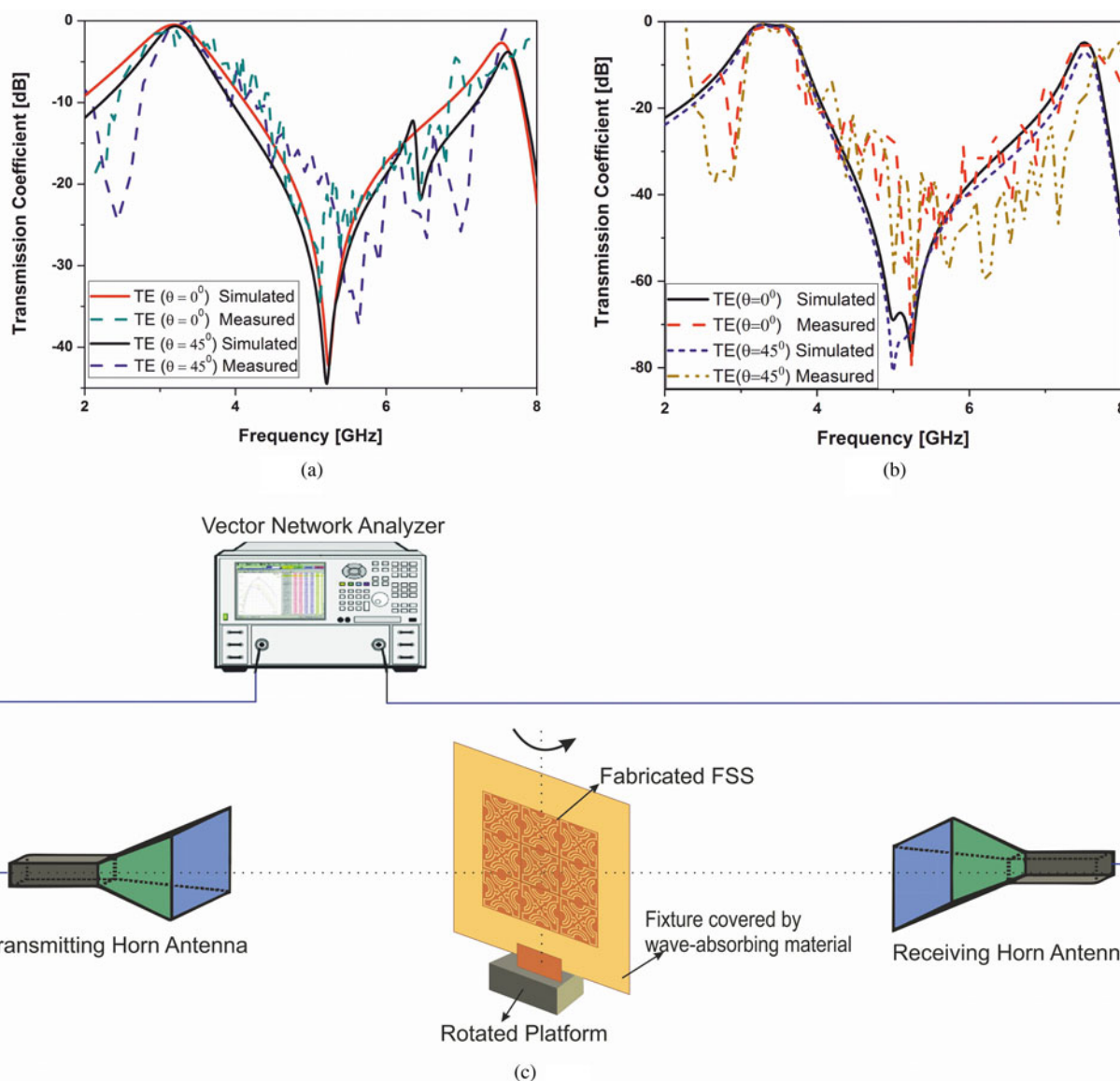


**Fig. 15.** Simulated vs Measured frequency response at various incident angles under TE polarization for (a) single layer (b) double layer CFSS and (c) Block diagram of the oblique incidence measurement setup.

**Table 4.** Comparison of proposed double-layer CFSS with previously published literature

FSS structure	Element size	Structure thickness	SF (−3 dB B.W./−10 dB B.W)	ROC (dB/GHz)	% of passband bandwidth	% of stopband bandwidth	No. of passband poles & No. of stopband zeros
Ref. [12]	$0.107\lambda_0 \times 0.107\lambda_0$	$0.147\lambda_0$	0.603	24.14	38.15	N/A	2 & 1
Ref. [15]	$0.33\lambda_0 \times 0.33\lambda_0$	$0.076\lambda_0$	0.785	17.5	82.6	N/A	3 & 1
Ref. [16]	$0.326\lambda_0 \times 0.326\lambda_0$	$0.087\lambda_0$	0.838	20	63	N/A	3 & 2
Ref. [24]	$0.2\lambda_0 \times 0.2\lambda_0$	$0.257\lambda_0$	0.710	23.65	15	N/A	3 & 1
Ref. [26]	$0.2\lambda_0 \times 0.2\lambda_0$	$0.22\lambda_0$	N/A	N/A	36	N/A	3 & N/A
Ref. [30]	$0.076\lambda_0 \times 0.076\lambda_0$	$0.038\lambda_0$	0.581	87.5	10.94	N/A	2 & 2
Ref. [33]	$0.076\lambda_0 \times 0.076\lambda_0$	$0.038\lambda_0$	0.589	60.34	10	N/A	2 & 2
Ref. [34]	$0.4\lambda_0 \times 0.4\lambda_0$	$0.027\lambda_0$	0.598	58.33	25	N/A	2 & 1
Ref. [37]	$0.33\lambda_0 \times 0.33\lambda_0$	$0.2\lambda_0$	0.388	72.16	20	1.17	2 & 1
Ref. [46]	$0.558\lambda_0 \times 0.558\lambda_0$	$0.14\lambda_0$	0.717	13.20	20.5	11.23	2 & 3
Ref. [47]	$0.072\lambda_0 \times 0.072\lambda_0$	$0.010\lambda_0$	0.465	29.17	22.56	N/A	1 & 1
Planar double layer CFSS (proposed)	$0.105\lambda_0 \times 0.105\lambda_0$	$0.098\lambda_0$	0.731	72.4	19.23	64.7	2 & 2

**Table 5.** Comparison of angular stability of the proposed double-layer CFSS with previous works

FSS Structure	Resonant frequency deviation of 45°	
	TE	TM
Ref. [16]	8.17%	3.99%
Ref. [24]	0.88%	2.13%
Ref. [33]	2.45%	2.46%
Ref. [34]	2.11%	N/A
Planer double layer CFSS (proposed)	0.44%	0.65%

and conformal modes are illustrated in Figs 13 and 14 respectively. Though the experimental ripple can be seen, yet the envelop of the experimental results are in good agreement with the simulated results. The comparative simulated and measured results of both the planar and conformal modes are listed in Table 3. The little discrepancy observed between simulated and measured responses in parametric comparison may be due to the fabrication error of complex structure and the free space measurement environment. Otherwise, the better parity of the measured and simulated results can be seen.

Figure 15 shows the angular stability for TE polarization at two incident angles,  $\theta = 0^\circ$  and  $45^\circ$  have been investigated experimentally. The wooden fixture with embedded CFSS array is angularly rotated horizontally to obtain the transmission coefficient response at  $\theta = 45^\circ$ . It can be observed that the single and the double layer passband and stopband do not change significantly. The double-layer angular transmission coefficient response provides a stable passband and good stopband. Besides, two transmission poles of the passband and two transmission zeros of the stopband can precisely be determined from the measured results. Moreover, the remarkable angular stability regarding measured ROC and SF

can also be observed where ROC = 68.3 dB/GHz and SF = 0.764 for  $\theta = 45^\circ$ .

### Comparison with previously reported designs

Comparative analysis of the proposed double-layered CFSS structure is tabulated with various earlier reported designs in Table 4. The excellence of this proposed structure lies in its wide second-order passband as well as stopband with improved roll-off and sharp selectivity. Another significant feature of this proposed design is its noticeable improvement in angular stability as compared with the early works is summarized in Table 5.

### Conclusion

Two CFSS structures are proposed and investigated in this article: one is the single metallic layered ultrathin CFSS and the other structure includes two ultrathin CFSS metallic array with different slotted geometry separated by air foam. The properly synthesized cascaded double-layer structure with optimized air gap is able to achieve a wide bandpass and band stop response with a sharp passband to stopband transition roll-off and significantly high selectivity. The influence of the air gap is also investigated to realize the controllable second-order passband and stopband characteristics. A comprehensive analysis and a structural synthesis have been done with the help of the precisely developed lumped ECM and the transmission line model for both the single and double layer planar structures. Furthermore, the angular stability of both the structures is analyzed to access their passband stopband stability under a large variation of incident angle. Moreover, the bending effect of both the flexible structures is also discussed along with the equivalent circuit analysis to ascertain their conformal features. All the proposed performance parameters are validated by measured results which ensure the compatibility of both the proposed structures in WiMAX and WLAN systems.

**Acknowledgements.** The authors would like to acknowledge Dr. Partha Pratim Sarkar, Dept. of Engg & Technological Studies, University of Kalyani, India for the measurements.

## References

1. Lockyer DS, Vardaxoglou JC and Simpkin RA (2000) Complementary frequency selective surfaces. *IEE Proceedings - Microwaves, Antennas and Propagation* **147**, 501.
2. Nauman M, Saleem R, Rashid AK and Shafique MF (2016) A miniaturized flexible frequency selective surface for X-band applications. *IEEE Transactions on Electromagnetic Compatibility* **58**, 419–428.
3. Yan M, Qu S, Wang J, Ma H, Zhang J, Wang W, Zheng L and Yuan H (2015) A single layer ultra-miniaturized FSS operating in VHF. *Photonics and Nanostructures - Fundamentals and Applications* **17**, 1–9.
4. Liu N, Sheng X, Fan J and Guo D (2017) A miniaturized FSS based on tortuous structure design. *IEICE Electronics Express* **14**, 20161129.
5. Yan M, Qu S, Wang J, Zhang J, Zhang A, Xia S and Wang W (2014) A novel miniaturized frequency selective surface with stable resonance. *IEEE Antennas and Wireless Propagation Letters* **13**, 639–641.
6. Liu N, Sheng X, Zhang C, Fan J and Guo D (2017) A miniaturized tri-band frequency selective surface based on convoluted design. *IEEE Antennas and Wireless Propagation Letters* **16**, 2384–2387.
7. Hong T, Wang M, Peng K, Zhao Q and Gong S (2020) Compact ultra-wideband frequency selective surface with high selectivity. *IEEE Transactions on Antennas and Propagation* **68**, 5724–5729.
8. Ghosh S and Srivastava KV (2017) An angularly stable dual-band FSS With closely spaced resonances using miniaturized unit cell. *IEEE Microwave and Wireless Components Letters* **27**, 218–220.
9. Sanz-Izquierdo B, Robertson JB, Parker EA and Batchelor JC (2011) Wideband FSS for electromagnetic architecture in buildings. *Applied Physics A* **103**, 771–774.
10. Jia M, He X, Yang Y, Hua B, Hu W and Qian X (2020) Wideband ultraminiaturised-element frequency selective surface based on interlocked 2.5-dimensional structures. *Progress in Electromagnetics Research* **88**, 37–42.
11. Tao K, Li B, Wu Q and Tang Y (2016) Multi-layer tri-band frequency selective surface using stepped- and uniform-impedance resonators. *Electronics Letters* **52**, 583–585.
12. Li B and Shen Z (2013) Angular-stable and polarization-independent frequency selective structure with high selectivity. *Applied Physics Letters* **103**, 171607.
13. Xie JM, Li B, Lyu YP and Zhu L (2020) Single- and dual-band high-order bandpass frequency selective surfaces based on aperture-coupled dual-mode patch resonators. *IEEE Transactions on Antennas and Propagation* **69**, 2130–2141.
14. Jia S, Xu B and Zheng T (2020) Design of a 3-d tunable band-stop frequency selective surface with wide tuning range. *Progress in Electromagnetics Research Letters* **92**, 9–16.
15. Jin C, Lv Q and Mittra R (2018) A Novel Wideband Frequency Selective Surface Design based on Cascaded Patch Resonators with a Slotted Ground. *IEEE International Symposium on Antennas and Propagation & USNC/URSI National Radio Science Meeting*, pp. 2039–3040.
16. Lv Q, Jin C, Zhang B and Mittra R (2019) Wide-passband dual-polarized elliptic frequency selective surface. *IEEE Access* **7**, 55833–55840.
17. Krushna Kanth V and Raghavan S (2020) Design and optimization of complementary frequency selective surface using equivalent circuit model for wideband EMI shielding. *Journal of Electromagnetic Waves and Applications* **34**, 51–69.
18. Xu N, Gao J, Zhao J and Feng X (2015) A novel wideband, low-profile and second-order miniaturized band-pass frequency selective surfaces. *AIP Advances* **5**, 077157.
19. Mellita RA, Chandu DS, Karthikeyan SS and Damodharan P (2020) A miniaturized wideband frequency selective surface with interconnected cell structure. *AEU-International Journal of Electronics and Communications* **120**, 153196.
20. Sivasamy R, Moorthy B, Kanagasabai M, Samsingh VR and Alstath MGN (2018) A wideband frequency tunable FSS for electromagnetic shielding applications. *IEEE Transactions on Electromagnetic Compatibility* **60**, 280–283.
21. Sarika MRT and Ronnow D (2018) A wideband frequency selective surface reflector for 4G/X-band/Ku-band. *Progress in Electromagnetics Research C* **81**, 151–159.
22. Zhang B, Jin C, Ye X and Mittra R (2018) Dual-Band dual-polarized quasi-elliptic frequency selective surfaces. *IEEE Antennas and Wireless Propagation Letters* **18**, 298–302.
23. Li B and Shen Z (2013) Synthesis of quasi-elliptic bandpass frequency-selective surface using cascaded loop arrays. *IEEE Transactions on Antennas and Propagation* **61**, 3053–3059.
24. Gao M, Abadi SMAMH and Behdad N (2017) A hybrid miniaturized-element frequency selective surface With a third-order bandpass response. *IEEE Antennas and Wireless Propagation Letters* **16**, 708–711.
25. Rashid AK, Li B and Shen Z (2014) An overview of three-dimensional frequency-selective structures. *IEEE Antennas and Propagation Magazine* **56**, 43–67.
26. Li Y, Li L, Zhang Y and Zhao C (2015) Design and synthesis of multilayer frequency selective surface based on antenna-filter-antenna using Minkowski fractal structures. *IEEE Transactions on Antennas and Propagation* **63**, 133–141.
27. Chatterjee A and Parui SK (2016) A dual layer frequency selective surface reflector for wideband applications. *Radioengineering* **25**, 67–72.
28. Yan M, Wang J, Qu S, Feng M, Li Z, Chen H, Zhang J and Zheng L (2016) Highly-selective, closely-spaced, dual-band FSS with second-order characteristic. *IET Microwaves, Antennas & Propagation* **10**, 1087–1091.
29. Gao C, Pu H, Gao S, Chen C and Yang Y (2020) Design and analysis of a tri-band frequency selective surface with a second-order response. *International Journal of Microwave and Wireless Technologies* **12**, 205–211.
30. Hussein M, Zhou J, Huang Y and Al-Juboori B (2017) A Low-profile miniaturized second-order bandpass frequency selective surface. *IEEE Antennas and Wireless Propagation Letters* **16**, 2791–2794.
31. Anwar RS, Wei Y, Mao L and Ning H (2019) Miniaturised frequency selective surface based on fractal arrays with square slots for enhanced bandwidth. *IET Microwaves, Antennas & Propagation* **13**, 1811–1819.
32. Li H and Cao Q (2015) Design and analysis of a controllable miniaturized tri-band frequency selective surface. *Progress in Electromagnetics Research Letters* **52**, 105–112.
33. Hussein MN, Zhou J, Huang Y, Kod M and Sohrab AP (2017) Frequency selective surface structure miniaturization using interconnected array elements on orthogonal layers. *IEEE Transactions on Antennas and Propagation* **65**, 2376–2385.
34. Krushna Kanth V and Raghavan S (2020) Ultrathin wideband slot and patch FSS elements with sharp band edge characteristics. *International Journal of Electronics* **107**, 1365–1385.
35. Yang XF, Wang L, Shen X, Liu X, Qi T and Zhou Y (2020) Single-substrate double-Side high selectivity frequency selective surface. *Progress in Electromagnetics Research Letters* **92**, 85–92.
36. Al-Joumayly MA and Behdad N (2010) Low-profile, highly-selective, dual-band frequency selective surfaces with closely spaced bands of operation. *IEEE Transactions on Antennas and Propagation* **58**, 4042–4050.
37. Wang HB and Cheng YJ (2016) Frequency selective surface with miniaturized elements based on quarter-mode substrate integrated waveguide cavity with two poles. *IEEE Transactions on Antennas and Propagation* **64**, 914–922.
38. Varikuntla KK and Singaravelu R (2019) Design of SIW cavity models to control the bandwidth of frequency selective surface. *IET Microwaves, Antennas & Propagation* **13**, 2515–2524.
39. Yong WY, Abdul Rahim SK, Himdi M, Seman FC, Suong DL, Ramli MR and Elmobarak HA (2018) Flexible convoluted ring-shaped FSS for X-band screening application. *IEEE Access* **6**, 11657–11665.
40. Gurrula P, Oren S, Liu P, Song J and Dong L (2017) Fully conformal square-patch frequency-selective surface toward wearable electromagnetic shielding. *IEEE Antennas and Wireless Propagation Letters* **16**, 2602–2605.
41. Kong X, Xu J, Mo J and Liu S (2017) Broadband and conformal metamaterial absorber. *Frontiers of Optoelectronics* **10**, 124–131.



42. **Pous R and Pozar DM** (1991) A frequency-selective surface using aperture-coupled microstrip patches. *IEEE Transactions on Antennas and Propagation* **39**, 1763–1769.
43. **Guo Q, Li Z, Su J, Song J and Yang LY** (2019) Active frequency selective surface with wide reconfigurable passband. *IEEE Access* **7**, 38348–38355.
44. **Lee IG, Park YB, Chun HJ, Kim YJ and Hong IP** (2017) Design of active frequency selective surface with curved composite structures and tunable frequency response. *International Journal of Antennas and Propagation* **2017**, Article ID 6307528, 10.
45. **Savia SB and Parker EA** (1999) Current distribution across curved ring element FSS. *IEEE National Conference on Antennas and Propagation*, pp. 332–335.
46. **Li D, Li TW, Hao R, Chen HS, Yin WY, Yu HC and Li EP** (2019) A low-profile broadband bandpass frequency selective surface with two rapid band edges for 5G near-field applications. *IEEE Transactions on Electromagnetic Compatibility* **59**, 670–676.
47. **Sheng X, Fan J, Liu N and Zhang C** (2017) A dual-band fractal FSS with SZ curve elements. *IEICE Electronics Express* **14**, 20170518–20170518.



**Srimita Coomar** has obtained her B.Tech and M.Tech degree in electronics & communication engineering from MCKV Institute of Engineering under MAKAUT, WB in the year 2016 and 2018 respectively. Currently, she is associated with the Institute of Radio Physics & Electronics, the University of Calcutta as a Ph.D. (Tech.) researcher. Her main research interests are frequency selective surfaces, microstrip antenna under the domain of RF & microwave.



**Dr. Santanu Mondal** obtained his M.E in ETCE from the University of Jadavpur and Ph.D. in Engineering from University of Kalyani. He earned his B.tech degree in ECE from Kalyani Govt. Engineering College under MAKAUT, WB. He is presently working as assistant professor at the Institute of Radio Physics & Electronics, University of Calcutta. His area of research includes planar monopole antenna, circularly polarized microstrip antenna, frequency selective surfaces, microwave absorber. He has contributed to various research articles in various journals and conferences of repute.



**Dr. Rajarshi Sanyal** has obtained his AMIETE and M.Tech degree in electronics and communication. He earned his Ph.D. in Engineering from the University of Kalyani. His area of research includes microstrip antenna, microstrip filters and frequency selective surfaces. Presently, he is working as assistant professor at MCKV Institute of Engineering. He has presented and published various research papers in national and international journals.